

# Star formation conditions in a Planck Galactic Cold Clump, G108.84-00.81

Jungha Kim<sup>1,2,3</sup>, Jeong-Eun Lee<sup>1</sup>, Tie Liu<sup>4</sup>, Kee-Tae Kim<sup>4</sup>, Yuefang Wu<sup>5</sup>, Ken'ichi,  
Tatematsu<sup>2,3</sup>, Sheng-Yuan Liu<sup>6</sup>, JCMT Large Program “SCOPE” collaboration, and  
TRAO Key Science Program “TOP” collaboration

<sup>1</sup> School of Space Research, Kyung Hee University, 1732, Deogyong-daero, Giheung-gu,  
Yongin-si, Gyeonggi-do, Korea

<sup>2</sup> Department of Astronomical Science, SOKENDAI (The Graduate University for  
Advanced Studies), 2-21-1 Osawa, Mitaka, Tokyo 181-8588, Japan

<sup>3</sup> National Astronomical Observatory of Japan, 2-21-1 Osawa, Mitaka, Tokyo 181-8588,  
Japan

<sup>4</sup> Korea Astronomy and Space Science Institute, 776 Daedeokdaero, Yuseong, Daejeon  
34055, Korea

<sup>5</sup> Department of Astronomy, Peking University, 100871, Beijing, China

<sup>6</sup> Academia Sinica, Institute of Astronomy and Astrophysics, P.O. Box 23-141, Taipei 106,  
Taiwan

Received \_\_\_\_\_; accepted \_\_\_\_\_

## ABSTRACT

We present the results from a series of ground-based radio observations toward a Planck Galactic Cold Clump (PGCC), PGCC G108.84–00.81, which is located in one curved filamentary cloud in the vicinity of an extended HII region Sh2-152 and SNR G109.1-1.0. PGCC G108.84–00.81 is mainly composed of two clumps, “G108–N” and “G108–S”. In the 850  $\mu\text{m}$  dust continuum emission map, G108–N is shown as one component while G108–S is fragmented into four components. There is no infrared source associated with G108–N while there are two infrared sources (IRS 1 and IRS 2) associated with G108–S. The total mass of G108–N is larger than the jeans mass, suggesting that G108–N is gravitationally unstable and a potential place for a future star formation. The clump properties of G108–N and G108–S such as the gas temperature and the column density, are not distinctly different. However, G108–S is slightly more evolved than G108–N, in the consideration of the CO depletion factor, molecular abundances, and association with infrared sources. G108–S seems to be affected by the compression from Sh2-152, while G108–N is relatively protected from the external effect.

## 1. INTRODUCTION

Expanding HII regions or supernova explosions can strongly influence their surrounding interstellar medium (ISM) and regulate star formation. The shocks induced in HII regions or supernova remnants may gather surrounding molecular gas to form dense shells, which may collapse to form stars later (Elmegreen & Lada 1977; Whitworth et al. 1994). This so-called “collect and collapse” process can self-propagate and lead to sequential star formation (Elmegreen & Lada 1977; Whitworth et al. 1994). The “collect and collapse” model was firstly developed to explain the age sequence of spatially distinct OB subgroups in nearby OB associations such as Orion OB1 (Elmegreen & Lada 1977). More and more evidences in recent observations indicate that new generation of stars can form in shells or pillar structures surrounding HII regions (see Liu et al. 2012a; Dale et al. 2015; Liu et al. 2015; Liu et al. 2016a and the references therein). Thompson et al. (2012) estimated that the fraction of massive stars in the Milky Way formed by triggering process could be between 14 and 30 % through statistical studies of young stellar objects (YSOs) projected against the rims of Spitzer infrared bubbles.

However, recent numerical simulations suggest that stellar feedback from massive stars always results in a lower star formation efficiency and most signs such as the ages and geometrical distribution of stars relative to the feedback source or feedback-driven structure (e.g. shells, pillar structures), may not be substantially helpful in distinguishing triggered star formation from spontaneous star formation (Dale et al. 2012, 2015). Studying the conditions (e.g., temperature, density, velocity, chemistry) of dense cores near HII regions may be helpful to distinguish triggered star formation from spontaneous star formation. The dense cores should be externally heated and compressed by HII regions if their star formation would be triggered.

The *Planck* satellite survey provides a catalog containing 13,188 Planck Galactic cold

clumps (PGCCs; Planck Collaboration et al. 2015). The clumps have dust temperatures lower than 14 K, indicating that PGCCs correspond to the coldest portion of the ISM. A survey in the  $J = 1-0$  lines of  $^{12}\text{CO}$ ,  $^{13}\text{CO}$ , and  $\text{C}^{18}\text{O}$  toward 674 PGCCs, has been carried out using the 13.7 m telescope of Purple Mountain Observatory (PMO) (Wu et al. 2012; Liu et al. 2013; Zhang et al. 2016). Nearly 98 % of the clumps have the excitation temperatures ( $T_{\text{ex}}$ ) of CO 1–0 lower than 16 K. Clumps with excitation temperatures above 16 K are located in star-forming regions, suggesting that the high  $T_{\text{ex}}$  is related to star-forming activities (Wu et al. 2012). A large fraction of PGCCs have lower temperatures than the typical temperature of Infrared dark clouds (IRDCs) (15 K; Pillai et al. 2006), which are known to be the earliest phase of star formation (Carey et al. 1998; Simon et al. 2006). It suggests that PGCCs may represent an earlier evolutionary stage than IRDCs. To investigate the initial conditions of star formation, and especially to study the environmental effect on dense core formation, a legacy survey of PGCCs using the Submillimeter Common User Bolometer Array-2 (SCUBA-2) on board of the James Clerk Maxwell Telescope (JCMT) at East Asia Observatory, “SCUBA-2 Continuum Observations of Pre-protostellar Evolution (SCOPE<sup>1</sup>)” is in progress (liu et al. 2017, in preparation).

PGCC G108.84–00.81 is observed as part of SCOPE. It has an excitation temperature of  $\sim 15$  K and  $\text{H}_2$  column density of  $2.0 \times 10^{22} \text{ cm s}^{-1}$  (Wu et al. 2012). Hereafter we call the region covered by PMO observations ( $500'' \times 500''$ ) as PGCC G108.84–00.81 and the central part of PGCC G108.84–00.81 covered by SCUBA-2 as G108. A supernova Remnant (SNR) G109.1–1.0 and an HII region, Sh2-152, are located near PGCC G108.84–00.81. Therefore, PGCC G108.84–00.81 is an ideal target to investigate the environmental effect on the initial conditions of star formation.

In this study, we investigate the interaction between PGCC G108.84–00.81 and its

---

<sup>1</sup><https://topscope.asiaa.sinica.edu.tw/tiki/tiki-index.php>

surrounding environments with CO line observations. The chemical and physical properties of G108 are also studied in detail through a series of observations in both continuum and molecular lines. In Section 2, our observations toward PGCC G108.84–00.81 and G108 are summarized. Results and analysis are presented in Section 3 and Section 4, respectively. We discuss the environmental influence on the star formation in PGCC G108.84–00.81 in Section 5. Finally, a summary of the study is given in Section 6.

## 2. THE DATA

A series of observations toward PGCC G108.84–00.81 have been conducted with ground-based radio telescopes. The reduction process of molecular line data was done using the GILDAS/CLASS<sup>2</sup> package. A summary of the molecular line observations is in Table 1.

### 2.1. PMO Observations

The CO 1–0, <sup>13</sup>CO 1–0, and C<sup>18</sup>O 1–0 line mapping observations of PGCC G108.84–00.81 were carried out using the 13.7 m radio telescope of the PMO at De Ling Ha in 2011 May. The On-The-Fly (OTF) observing mode was applied. More details of the OTF observations with the PMO 13.7 m telescope toward Planck cold clumps can be found in Liu et al. (2012). The beam Full Width at Half Maximum (FWHM) is  $\sim 52''$  at 115 GHz and the beam efficiency is  $\sim 0.45$ . Newly installed nine-beam array receiver in the single-sideband mode was used. The Fast Fourier Transform Spectrometer (FFTS), which has 16,384 channels in a total bandwidth of 1 GHz, were used. The velocity resolution of the CO 1–0 line is  $0.16 \text{ km s}^{-1}$  and that of both <sup>13</sup>CO 1–0 and C<sup>18</sup>O 1–0 is  $0.17 \text{ km s}^{-1}$ .

---

<sup>2</sup>see <http://www.iram.fr/IRAMFR/GILDAS/doc/html/class-html/class.html>.

CO 1–0 was observed at the upper sideband and  $^{13}\text{CO}$  1–0 and  $\text{C}^{18}\text{O}$  1–0 were observed simultaneously at the lower sideband. The map size for further analysis is about  $480'' \times 480''$ .

## 2.2. CSO Observations

Molecular line observations of PGCC G108.84–00.81 were carried out with the 10 m telescope of the Caltech Submillimeter Observatory (CSO) in 2014 January (see Meng et al. in preparation). We mapped the CO 2–1,  $^{13}\text{CO}$  2–1, and  $\text{C}^{18}\text{O}$  2–1 lines toward G108. The Sidecab receiver and the FFTS2 spectrometer were used. The velocity resolution is about  $0.35 \text{ km s}^{-1}$ . The beam FWHM is  $32.5''$  and the beam efficiency is 0.76 at 230 GHz. A map area of  $120'' \times 120''$  centered at G108 is selected for further analysis because of apparent higher noise levels at map edges.

## 2.3. NRO Observations

The northern part and the southern part of G108 were observed separately with the 45 m radio telescope of the Nobeyama Radio Observatory (NRO) in 2015 December. We observed  $\text{N}_2\text{H}^+$  1–0 with the TZ1 receiver. The velocity resolution is about  $0.2 \text{ km s}^{-1}$ . The beam FWHM at 93 GHz is  $20.4''$  and the beam efficiency is 0.54. Each mapped area toward the northern and southern part of G108 is  $50'' \times 50''$ .

## 2.4. IRAM Observations

We also observed the  $\text{HCO}^+$  1–0 and HCN 1–0 lines toward the northern part of G108 with the 30 m radio telescope of the Institut de Radioastronomie Millimétrique (IRAM) in 2014 May. The velocity resolution is  $0.33 \text{ km s}^{-1}$ . The beam FWHM and beam efficiency

are  $\sim 29''$  and 0.81, respectively. The map size is  $80'' \times 80''$ .

## 2.5. Effelsberg Observations

Observations of the northern part of G108 in the  $\text{NH}_3$  (1,1) line was carried out with the 100 m radio telescope of Effelsberg in 2015 April. The  $\text{NH}_3$  (1,1) line was observed with 1.3 cm double beam secondary focus receiver. The beam FWHM and beam efficiency are  $\sim 38''$  and 0.79, respectively. The velocity resolution is  $0.15 \text{ km s}^{-1}$ . An area of  $80'' \times 80''$  was mapped.

## 2.6. KVN Observations

Single-point observations of the HCN 1–0 line were carried out toward the peak positions of the  $850 \mu\text{m}$  dust continuum map in 2016 June with the Korean VLBI Network (KVN) 21 m telescopes (Kim et al. 2011). Observations were conducted at the three stations of KVN (Yeonsei, Ulsan, and Tamna). We used the digital spectrometer with 32 MHz in bandwidth divided into 4096 channels, providing velocity resolution of  $\sim 0.2 \text{ km s}^{-1}$  at 88 GHz. The averaged beam FWHM and beam efficiency at the three stations are  $\sim 32''$  and  $\sim 0.39$  at 88 GHz, respectively.

## 2.7. JCMT Observations

The  $850 \mu\text{m}$  continuum emission map was obtained with JCMT/SCUBA-2 in 2015 May in the "CV Daisy" mapping mode, which is optimised for point sources. The CV Daisy is designed for small compact sources providing a deep  $3'$  region in the centre of the map but coverage out to beyond  $12'$  (Bintley et al. 2014). All the SCUBA-2  $850 \mu\text{m}$

continuum data were reduced using an iterative map-making technique (Chapin et al. 2013). Specifically the data were all run with the reduction tailored for compact sources, filtering out scales larger than  $200''$  on a  $4''$  pixel scale. The beam FWHM of SCUBA-2 at  $850\ \mu\text{m}$  is  $\sim 13''$ . The field of view of SCUBA-2 is about  $8'$  at  $850\ \mu\text{m}$ . However, an area of about  $5' \times 5'$  centered at PGCC G108.84–00.81 is used for further analysis.

Molecular line observations in  $\text{HCO}^+$  4–3 toward the northern part of G108 were also carried out using the JCMT Heterodyne Array Receiver Program (HARP) system in 2015 September. HARP is a Single Sideband array receiver composed of 16 SIS mixers. The beam FWHM at 350 GHz is  $\sim 14''$  and the beam efficiency is 0.64. The mapping area is about  $50'' \times 50''$ . We used the "ORAC-DR" pipeline in STARLINK for imaging data reduction.

## 2.8. Infrared Data

We also included images from *Wide-field Infrared Survey Explorer* (WISE) (Wright et al. 2010). We gathered available photometric data of Young Stellar Object (YSO) candidates in G108 from several catalogs. The data at 3.4, 4.6, 12, and  $22\ \mu\text{m}$  are from the ALLWISE catalog including 2MASS data. The data at 9 and  $18\ \mu\text{m}$  are from the AKARI/IRC Point Source Catalogue (AKARIPSC; Ishihara et al. 2010).

## 3. RESULTS

### 3.1. Filament structure in the CO 1–0 and $^{13}\text{CO}$ 1–0 maps

PGCC G108.84–00.81 is surrounded by dynamically active regions such as a supernova remnant, SNR G109.1–1.0, and an HII region, Sh2-152. According to Planck Early Cold



Clump catalog note<sup>3</sup>, there is one IRAS point source, IRAS 22565+5839, associated with PGCC G108.84–00.81 within 5 arcmin from the center of PGCC G108.84–00.81. One large filament structure is shown in the integrated intensity map of CO 1–0 (Figure 1).

This filament structure is largely divided into three parts: the northeast region associated with a star (Yung et al. 2014), IRAS 22576+5843, the southern region directly linked to Sh2-152, and the central part defined as G108, containing IRAS 22565+5839. As shown in the <sup>13</sup>CO 1–0 map in Figure 2, G108 is composed of two components. One is located at northeast (NE) from the central position and the other is located at southwest (SW). We use “G108–N” to indicate the NE component and “G108–S” for the SW component.

The systemic velocity of  $-49.6 \text{ km s}^{-1}$  has been measured by Gaussian fitting the C<sup>18</sup>O 1–0 spectra toward G108. The nearby HII region, Sh2-152, has a similar systemic velocity to G108. We adopt the distance to PGCC G108.84–00.81 as  $3.21 \pm 0.21 \text{ kpc}$  from the distance estimation of Sh2-152 by Ramírez Alegría et al. (2011) based on near-infrared extinction. According to the moment 1 maps presented in Figure 2, a small velocity gradient is present at the SW part of PGCC G108.84–00.81.

### 3.2. Two clumps within G108

Figure 3 presents the integrated intensity maps of CO 2–1 and <sup>13</sup>CO 2–1 overlaid onto their Moment 1 maps obtained at the CSO. G108–N and G108–S seem separated in the CO 2–1 map. The integrated intensity map of <sup>13</sup>CO 2–1 presents more fragmented structures than that of CO 2–1. The component with a blue-shifted velocity with regard to the systemic velocity ( $\sim -50.5 \text{ km s}^{-1}$ ), is shown in the west of G108–S. The red-shifted

---

<sup>3</sup><http://irsa.ipac.caltech.edu/Missions/planck.html>

velocity components are located along the eastern edge of filament in the  $^{13}\text{CO}$  2–1 map.

The spectra of CO isotopologues obtained with the CSO telescope toward G108–N and G108–S are shown in Figure 4. The central velocities of three lines are coincident with each other. Figure 5 shows the integrated intensity ratios, CO 2–1/CO 1–0 and  $^{13}\text{CO}$  2–1/ $^{13}\text{CO}$  1–0. The enhancement of CO 2–1/CO 1–0 ratios ( $> 1$ ) are known toward molecular clouds associated with SNRs (Seta et al. 1998). However, in G108, the  $^{13}\text{CO}$  2–1/ $^{13}\text{CO}$  1–0 ratio is the most enhanced at the southern edge of G108–S, which is close to the HII region.

In Figure 6, the 850  $\mu\text{m}$  dust continuum emission map is overlaid onto the WISE 12  $\mu\text{m}$  image. Dust continuum emission toward G108 is also largely divided into two parts (G108–N and G108–S), as molecular line emission. Distribution of dust continuum emission of G108–N shows a cometary structure. The head is located at the NE from the center with a tail structure extended to SW. Highly fragmented structure appears in G108–S. At least four components exist in G108–S. G108–S1 to S4 are assigned along with Right Ascension. As shown in the integrated intensity maps of CO 2–1,  $^{13}\text{CO}$  2–1, and  $\text{C}^{18}\text{O}$  2–1 overlaid onto the 850  $\mu\text{m}$  dust continuum emission map (Figure 7), the intensity peaks of all three lines are off from that of the dust continuum.

### 3.3. A starless clump, G108–N

To investigate the molecular environments of the starless clump, G108–N, single-dish observations were conducted. The integrated intensity maps of  $\text{HCO}^+$  1–0 and HCN 1–0 obtained with the IRAM 30 m telescope are shown in Figure 8. The  $\text{HCO}^+$  1–0 and HCN 1–0 show a similar distribution to each other and also to the distribution of 850  $\mu\text{m}$  continuum emission. The peak positions of  $\text{HCO}^+$  1–0 and HCN 1–0 are slightly shifted from that of the 850  $\mu\text{m}$  continuum emission peak. The emission of the two lines distributes

along the cometary structure in the NE-SW direction. The head at the NE with a tail extended to SW is shown in  $\text{HCO}^+$  1–0 and  $\text{HCN}$  1–0 maps while  $\text{HCO}^+$  4–3 obtained with the JCMT/HARP shows a compact distribution near the head part (Figure 8c). This cometary structure is also shown in the integrated intensity map of  $\text{NH}_3$  (1,1) obtained with the Effelsberg 100 m telescope (Figure 9).

The line profiles of all observed molecular lines toward the  $850 \mu\text{m}$  dust continuum peak of G108–N are presented in Figure 10. The centroid velocities of all lines are consistent.

## 4. ANALYSIS

### 4.1. IR source in association with G108

G108–N has no associated infrared (IR) source. On the other hand, two IR sources associated with G108–S1 and G108–S2 are detected at all four bands of WISE (Figure 6). Hereafter, the IR sources associated with G108–S1 and G108–S2 are called IRS 1 and IRS 2, respectively. IRAS 22565+5839, an associated IRAS point source from the PGCC catalog, is located at the center of the projected separation of IRS 1 and IRS 2, suggesting that the IRAS source is resolved at the WISE  $12 \mu\text{m}$  with a higher spatial resolution ( $\sim 6''$ ). IRS 1 and IRS 2 are identified as YSO candidates based on the diagnostic color-color and color-magnitude diagrams (See Figure 11) in the YSO identification schemes presented by Koenig & Leisawitz (2014).

The evolutionary stages of IRS 1 and IRS 2 are classified by their spectral indices and bolometric temperatures. A spectral index  $\alpha$  is derived by fitting the photometric data in the wavelength range from 2 to  $24 \mu\text{m}$  as the following (Evans et al. 2009);

$$\alpha = \frac{d \log(\lambda S(\lambda))}{d \log(\lambda)}. \quad (1)$$

Here,  $S(\lambda)$  is the flux density at the wavelength  $\lambda$ . The photometric data used to estimate the spectral index are listed in Table 2. The spectral indices of IRS 1 and IRS 2 are 0.61 and 0.48, respectively. Using the classification scheme from Evans et al. (2009) (i.e., Class I for  $0.3 \leq \alpha$ , Flat for  $-0.3 \leq \alpha < 0.3$ , Class II for  $-1.6 \leq \alpha < -0.3$ , and Class III for  $\alpha < -1.6$ ), both are classified as Class I sources.

The bolometric luminosities ( $L_{\text{bol}}$ ) and bolometric temperatures ( $T_{\text{bol}}$ ) of the two YSO candidates are also calculated. The  $L_{\text{bol}}$  of IRS 1 and IRS 2 are 27 and 30  $L_{\odot}$ , respectively, indicating these two sources are low-mass YSOs ( $L_{\text{bol}} < 50 L_{\odot}$ ). IRS 1 and IRS 2 have  $T_{\text{bol}}$  of 341 K and 614 K, respectively. Following the classification criteria from Myers & Ladd (1993) (i.e., Class 0 for  $T_{\text{bol}} < 70$  K, Class I for  $70 \text{ K} \leq T_{\text{bol}} \leq 650$  K, and Class II for  $650 \text{ K} < T_{\text{bol}} \leq 2800$  K), both are also classified as Class I sources. The CO outflows, which are commonly associated with embedded Class 0/I sources, are not detected in these two Class I sources. Higher resolutions and better sensitivities may reveal the associated outflows. The bolometric luminosities, the bolometric temperatures, and the spectral indices of the two IR sources are listed in Table 3.

## 4.2. Clump properties of G108–N and G108–S

### 4.2.1. Gas temperature

We assume that the  $^{12}\text{CO}$  line is optically thick and all levels are in local thermodynamic equilibrium (LTE) to derive its excitation temperature (Liu et al. 2013). Therefore, the excitation temperatures ( $T_{\text{ex}}$ ) in all levels and the kinetic temperature ( $T_{\text{kin}}$ ) are the same. We also assume that dust and gas are well coupled ( $T_{\text{ex}} = T_{\text{kin}} = T_{\text{dust}}$ ).

The excitation temperature is derived from the brightness temperature of CO 2–1,

which is optically thick ( $\tau_\nu \gg 1$ ). The expression for the brightness temperature,  $T_b$  is:

$$T_b = [J_\nu(T_{\text{ex}}) - J_\nu(T_{\text{bg}})](1 - e^{-\tau_\nu})f, \quad (2)$$

where  $J_\nu = h\nu_u/k(e^{h\nu_u/kT} - 1)^{-1}$ ,  $\tau_\nu$  is optical depth, and  $f$  is the beam filling factor and assumed as unity.

We compared the calculated  $T_{\text{ex}}$  with the result of the previous studies. The mean  $T_{\text{ex}}$  toward G108–N and G108–S are 13.4 K and 12.5 K, respectively, which are consistent with the  $T_{\text{dust}}$  ( $11.9 \pm 2.8$  K) of PGCC G108.84–00.81 from the Planck PGCC catalog (Planck Collaboration et al. 2015).  $T_{\text{kin}}$  from the ammonia observations (Tatematsu et al. 2017) of G108–N and G108–S are 14.3 K and  $< 19.1$  K, respectively. The calculated  $T_{\text{ex}}$  is also consistent with this  $T_{\text{kin}}$ , suggesting that our LTE assumption is reliable.

#### 4.2.2. $H_2$ Column Density derived from $C^{18}O$ 2-1 line

We calculate the  $H_2$  column density from the  $C^{18}O$  line assuming LTE and the same excitation temperature as CO. The column density,  $N_{\text{thin}}$ , under the assumption of optically thin emission ( $\tau \ll 1$ ) can be estimated with the integrated intensity of the line integral  $W$  ( $\text{K km s}^{-1}$ ) (Schnee et al. 2007) as the following,

$$N_{\text{thin}} = \frac{8\pi W}{\lambda^3 A} \frac{g_l}{g_u} \frac{1}{J_\nu(T_{\text{ex}}) - J_\nu(T_{\text{bg}})} \frac{1}{1 - \exp(-h\nu/kT_{\text{ex}})} \frac{Q_{\text{rot}}}{g_l \exp(-E_l/kT_{\text{ex}})} \text{cm}^{-2} \quad (3)$$

where  $\nu$  and  $\lambda$  are the frequency and wavelength of the transition,  $A$  is the Einstein coefficient,  $g_l$  and  $g_u$  are the statistical weights of the lower and the upper levels,  $J_\nu(T) = \frac{h\nu/k}{e^{h\nu/kT} - 1}$ ,  $Q_{\text{rot}}$  is the partition function, and  $E_l$  is the energy of the lower level. The energy of the each level is given by  $E_J = J(J + 1)hB$  where  $B$  is the rotational constant.

However, in some cases,  $C^{18}O$  2–1 is not perfectly optically thin. An optical depth can be corrected in the calculation of column density by using the correction factor,  $C_\tau$ , as long

as  $\tau \leq 2$  (Schnee et al. 2007).

$$C_\tau = \frac{\tau}{1 - e^{-\tau}}. \quad (4)$$

The optical depth ( $\tau$ ) can be found from

$$\tau = -\ln \left[ 1 - \frac{T_{\text{thin}}}{J(T_{\text{ex}}) - J(T_{\text{bg}})} \right], \quad (5)$$

where  $T_{\text{thin}}$  is the beam corrected brightness temperature of the given line. The final column density corrected for the optical depth is

$$N = N_{\text{thin}} \cdot C_\tau. \quad (6)$$

Finally, the  $\text{H}_2$  column density is derived by dividing the abundance of the molecule  $x$ ,  $X(x)$ :

$$N(\text{H}_2) = \frac{N(x)}{X(x)} \text{ cm}^{-2} \quad (7)$$

The  $\text{C}^{18}\text{O}$  abundance,  $X(\text{C}^{18}\text{O})$ , of  $4.8 \times 10^{-7}$  is used (Lee et al. 2003).

The sizes of G108–N and G108–S are defined as  $R = \sqrt{a \cdot b}$ , where  $a$  and  $b$  are the major and minor axes of deconvolved FWHM size measured at the 50 % contours of the  $\text{C}^{18}\text{O}$  2–1 emission region. The mean  $\text{H}_2$  column densities of G108–N and G108–S within the clump size are  $6.7 \times 10^{21}$  and  $1.0 \times 10^{22} \text{ cm}^{-2}$ , respectively. Derived parameters are listed in Table 4.

#### 4.2.3. $\text{H}_2$ column density derived from dust continuum emission

The molecular gas column density can be calculated with the dust continuum flux,  $S_\nu$ , using

$$N(\text{H}_2) = \frac{S_\nu}{\mu m_{\text{H}} \kappa_\nu B_\nu(T_{\text{dust}}) \Omega} \text{ cm}^{-2} \quad (8)$$

where  $\mu$  is the mean molecular weight,  $m_{\text{H}}$  is the atomic hydrogen mass,  $\kappa_\nu$  is the mass opacity coefficient, and  $B_\nu(T_{\text{dust}})$  is the Planck function with a dust temperature ( $T_{\text{dust}}$ ).

The dust temperature  $T_{\text{dust}}$  is adopted from the gas temperature derived in Section 4.2.1. The aperture solid angle,  $\Omega = \pi\theta^2/4\ln 2$  is a circular Gaussian aperture where  $\theta$  is the beam FWHM. We use the 850  $\mu\text{m}$  dust continuum emission to calculate the  $\text{H}_2$  column density. The mass opacity coefficient of  $0.018 \text{ cm}^2 \text{ g}^{-1}$  (Ossenkopf & Henning 1994) is used, by assuming a gas-to-dust ratio of 100. In order to make a consistent comparison, the 850  $\mu\text{m}$  data have been smoothed to the  $\text{C}^{18}\text{O}$  2–1 resolution. A beam FWHM of  $32.5''$  is used to calculate the aperture solid angle. Within the clump size, the mean  $\text{H}_2$  column densities of G108–N and G108–S are  $5.6 \times 10^{21}$  and  $8.4 \times 10^{21} \text{ cm}^{-2}$ , respectively. Derived parameters are also listed in Table 4.

#### 4.2.4. Total mass and kinematics

Dust continuum emission at 850  $\mu\text{m}$  is known as one of the best tracers of the total cloud mass because it is optically thin. Therefore, we derive the total (gas+dust) masses,  $M_{\text{total}}$ , of G108–N and G108–S, using

$$M_{\text{total}} = \frac{S_\nu d^2}{\kappa_\nu B_\nu(T_{\text{dust}})}, \quad (9)$$

where  $S_\nu$  is the 850  $\mu\text{m}$  integrated flux and  $d$  is the distance ( $3.21 \pm 0.21 \text{ kpc}$ ; Ramírez Alegría et al. 2011). We adopt the same coefficient as those used in Equation (8).  $T_{\text{dust}}$  for G108–N and G108–S are adopted from the gas temperature derived in Section 4.2.1. as 13.4 and 12.5 K, respectively. Their derived total masses are listed in Table 5. The total mass of G108–N is larger than the sum of the masses of G108–S1 to S4; the total mass of G108–N is  $386 \pm 2 M_\odot$ , indicative of a massive starless clump.

To investigate whether the clump is gravitationally unstable, and thus, the possibility of future star formation, we compare its Jeans mass with the total clump mass. The gas in molecular clouds is supported against gravitational collapse by turbulence and magnetic

field as well as the thermal pressure. The Jeans mass can be derived by

$$M_J \approx \left( \frac{T_{\text{eff}}}{10 \text{ K}} \right)^{\frac{3}{2}} \left( \frac{\mu}{2.33} \right)^{-\frac{1}{2}} \left( \frac{n}{10^4 \text{ cm}^{-3}} \right)^{-\frac{1}{2}} M_{\odot}, \quad (10)$$

taking into account the thermal and turbulent support (Hennebelle & Chabrier 2008), where  $n = N(H_2)/2R$  is the volume density of  $H_2$ . The effective kinematic temperature,  $T_{\text{eff}}$ , is given by

$$T_{\text{eff}} = C_{s,\text{eff}}^2 \mu m_{\text{H}} / k \quad (11)$$

with the effective sound speed  $C_{s,\text{eff}}$ . The  $C_{s,\text{eff}}$  including thermal and turbulent support can be derived by

$$C_{s,\text{eff}} = [(\sigma_{\text{NT}})^2 + (\sigma_{\text{T}})^2]^{\frac{1}{2}}. \quad (12)$$

The one-dimensional thermal ( $\sigma_{\text{T}}$ ) and non-thermal ( $\sigma_{\text{NT}}$ ) velocity dispersions can be calculated as follows,

$$\sigma_{\text{T}} = \left[ \frac{kT_{\text{ex}}}{m_{\text{H}}\mu} \right]^{\frac{1}{2}} \quad (13)$$

$$\sigma_{\text{NT}} = \left[ \sigma_{\text{C}^{18}\text{O}}^2 - \frac{kT_{\text{ex}}}{m_{\text{C}^{18}\text{O}}} \right]^{\frac{1}{2}}, \quad (14)$$

where  $k$  is the Boltzmann's constant.  $\sigma_{\text{C}^{18}\text{O}}^2 = \Delta V_{\text{C}^{18}\text{O}}^2 / 8 \ln(2)$  is the one-dimensional velocity dispersion of  $\text{C}^{18}\text{O}$  2–1 and  $m_{\text{C}^{18}\text{O}}$  is the mass of  $\text{C}^{18}\text{O}$ . The calculated Jeans mass is  $299 M_{\odot}$  with  $n = 1.0 \times 10^3 \text{ cm}^{-3}$ ,  $T_{\text{eff}} = 222 \text{ K}$ ,  $\sigma_{\text{T}} = 0.20 \text{ km s}^{-1}$ , and  $\sigma_{\text{NT}} = 0.79 \text{ km s}^{-1}$ . The total mass of G108–N ( $386 M_{\odot}$ ) is larger than  $M_J$ , suggesting that G108–N is gravitationally unstable (i.e., a prestellar clump).

### 4.3. Chemical status of two clumps

#### 4.3.1. CO depletion

According to the comparison between the integrated intensity distributions of molecular lines and dust continuum, the molecular line emission peaks are slightly shifted to SW from



the dust continuum emission peak. This might be caused by the molecular depletion at the dust continuum peak (Lee et al. 2003). We compare the  $\text{H}_2$  column densities,  $N(\text{H}_2)$ , derived from  $\text{C}^{18}\text{O}$  2–1 and the 850  $\mu\text{m}$  dust continuum emission to derive the CO depletion factor, which is defined as:

$$D_{\text{co}} = \frac{N(\text{H}_2)_{\text{dust}}}{N(\text{H}_2)_{\text{C}^{18}\text{O}}}. \quad (15)$$

The maximum depletion factor of G108–N is about 1.8 while that of G108–S is about 4. The low CO depletion suggests that the dynamical timescales of G108–N and G108–S are not very large, that is, the high-density clumps might form recently. However, we cannot rule out an artificial effect; the  $\text{H}_2$  column density derived from dust continuum emission could be underestimated because the extended structure is possibly filtered out during the reduction process.

#### 4.3.2. Molecular abundances

Figure 12 shows the averaged spectra within the 50 % contour of integrated intensity peak of  $\text{N}_2\text{H}^+$  1–0 towards G108–N and G108–S obtained with the NRO 45 m telescope; the  $\text{N}_2\text{H}^+$  1–0 emission is spatially distributed in larger area than the beam FWHM (20.4"). The  $\text{N}_2\text{H}^+$  1–0 line is fitted using the hyperfine structure (HFS) fitting method in GILDAS/CLASS to determine  $T_{\text{ex}}$  and optical depth,  $\tau$ . In both clumps, the  $\text{N}_2\text{H}^+$  1–0 lines are optically thin ( $\tau < 0.1$ ). Derived  $T_{\text{ex}}$  of G108–N and G108–S are 3.7 and 3.3 K, respectively, which are very low, compared to the  $T_{\text{ex}}$  of CO in G108–N (13.4 K) and G108–S (12.5 K). We also derived the  $T_{\text{ex}}$  of HCN by fitting the HFS of the HCN 1–0 line. The spectra of HCN 1–0 at each positions are presented in Figure 13. The  $T_{\text{ex}}$  of HCN in G108–N and G108–S are 3.6 and 3.8 K, respectively, which are similar to those of  $\text{N}_2\text{H}^+$ . The optical depths at all five positions are less than 1.

$\text{N}_2\text{H}^+$  and HCN seem sub-thermally excited, so we derive column density of  $\text{N}_2\text{H}^+$  and HCN using a non-LTE radiative transfer code, RADEX (van der Tak et al. 2007). We assume that  $T_{\text{kin}}$  is equal to  $T_{\text{ex}}$  derived from  $\text{C}^{18}\text{O}$  2–1 for G108–N and G108–S. The mean  $\text{H}_2$  volume density is derived from the 850  $\mu\text{m}$  dust continuum emission. For the  $\text{N}_2\text{H}^+$  analysis, the 850  $\mu\text{m}$  dust continuum map is convolved with the beam FWHM of NRO 45 m. The line widths of isolated component of  $\text{N}_2\text{H}^+$  1–0 ( $F_1, F = 0, 1 \rightarrow 1, 2$ ) of 1.72 and 2.67  $\text{km s}^{-1}$  for G108–N and G108–S, respectively, are used. Calculated  $\text{N}_2\text{H}^+$  1–0 column densities of G108–N and G108–S are  $1.2 \times 10^{14}$  and  $1.9 \times 10^{14} \text{ cm}^{-2}$ , respectively.  $T_{\text{ex}}$  from non-LTE calculation are 3.1 and 3.0 K for G108–N and G108–S, respectively, which are consistent with the result from the hyperfine structure (HFS) fitting method. The optical depth, however, calculated using non-LTE method are larger than that calculated by the HFS fitting. Fractional abundance of molecule  $x$ ,  $X(x)$ , can be derived as follows,

$$X(x) = N(x)/N(\text{H}_2)_{\text{dust}}. \quad (16)$$

The fractional abundances of  $\text{N}_2\text{H}^+$  1–0 are  $1.2 \times 10^{-8}$  and  $2.5 \times 10^{-8}$  for G108–N and G108–S, respectively. G108–N and G108–S have higher fractional abundances than previously studied dense cores ( $X(\text{N}_2\text{H}^+) \sim 1 \times 10^{-10}$ ) by Caselli et al. (2002), Tafalla et al. (2002), and Di Francesco et al. (2004). On the other hand, the  $\text{N}_2\text{H}^+$  1–0 fractional abundances of two clumps are consistent with those of cores within “Clump–S” of PGCC G192.32–11.88 (Liu et al. 2016), which are calculated in the assumption of LTE. The  $T_{\text{ex}}$  of cores in “Clump–S” is about 5 K and the optical depths is about 4. Derived parameters using  $\text{N}_2\text{H}^+$  1–0 are listed in Table 6.

For the non-LTE analysis of HCN 1–0, the 850  $\mu\text{m}$  dust continuum map is convolved with the beam FWHM of KVN 21 m to derive the  $\text{H}_2$  volume density. The HCN 1–0 spectra at the positions of the 850  $\mu\text{m}$  emission peaks are presented in Figure 11. The line width of the strongest component of HCN 1–0 is used. We average the four values for G108–S1,

S2, S3, and S4 as a representative value for G108-S for the consistency with the  $\text{N}_2\text{H}^+$  analysis.  $T_{\text{ex}}$  from the non-LTE calculation for HCN 1–0 are 3.8 and 4.0 K toward G108–N and G108–S, respectively. The column densities of HCN 1–0 in G108–N and G108–S are  $7.8 \times 10^{14}$  and  $6.5 \times 10^{14} \text{ cm}^{-2}$ , respectively. The optical depth from the non-LTE method are larger than that from the HFS analysis. The fractional abundances of HCN 1–0 are  $3.9 \times 10^{-7}$  and  $2.9 \times 10^{-7}$  for G108–N and G108–S, respectively. Derived parameters with HCN 1–0 are listed in Table 7.

## 5. DISCUSSIONS

PGCC G108.84–00.81 is located close to dynamically active regions such as an HII region (Sh2-152) and a SNR (SNR G109.1–1.0). SNR G109.1–1.0 is located at the east of PGCC G108.84–00.81. A line profile composed of two components, a sharp single peaked component with a broad component, was shown in the interacting regions between CO molecular clouds and SNRs (Seta et al. 1998; Su et al. 2014). So, the association between SNR G109.1–1.0 and CO molecular cloud in the vicinity of the remnant has been previously investigated (Tatematsu et al. 1987, 1990). However, according to Tatematsu et al. (1990), any broad CO emission, which is possibly accelerated by SNR G109.1–1.0, was not detected.

The channel map of CO 1–0 line emission of PGCC G108.84–00.81 are shown in Figure 14. The CO emission distributes along two filaments. A thin filament to the east is seen from  $-55$  to  $-52 \text{ km s}^{-1}$ . The main filament, which includes G108–N and G108–S, is seen from  $-52$  to  $-46.5 \text{ km s}^{-1}$ . The two filaments may be interacting in the north-east region, where IRAS 22576+5843 is located. However, the broad CO emission, which could be a hint for the interaction, does not appear. The thin filament is located in front of the main filament and seems to make a shield against the SNR shocks. As mentioned in section 3.2, CO 2–1/CO 1–0 ratios along the main filament are not enhanced by shocks. Therefore, the

main filament seems unaffected by the SNR.

However, the star formation in G108–S seems affected by the southern HII region, Sh2-152; G180–S is bent probably due to external compression by Sh2-152 and the CO 2–1/CO 1–0 ratio is enhanced at the bent region (see Figure 5). The gravitational collapse and fragmentation of G108–S might be induced by Sh2-152. G108–S is more evolved than G108–N. G108–N is a massive prestellar clump while G108–S is fragmented into 4 cores at least, G108–S1, G108–S2, G108–S3, and G108–S4, and G108–S1 (IRS 1) and G108–S2 (IRS 2) are associated with Class I sources. The overall clump properties of G108–N and G108–S are similar, and their chemical status does not show significant difference; G108–S is slightly more evolved than G108–N in the view of CO depletion.

By comparing the pressures of G108–S and Sh2-152, one can investigate whether the evolution of G108–S has been affected by Sh2-152. The internal pressure of Sh2-152 can be derived using (Morgan et al. 2004)

$$\frac{P_{\text{HII}}}{k} = 2n_e T_e. \quad (17)$$

The effective electron temperature  $T_e$  is assumed to be  $10^4$  K. For the electron density, the peak value ( $n_e = 2000 \text{ cm}^{-3}$ ) from Heydari-Malayeri & Testor (1981) is used. The derived  $P_{\text{HII}}/k$  is  $4.0 \times 10^7 \text{ cm}^{-3} \text{ K}$ . On the other hand, the molecular pressure inside G108–S is (Liu et al. 2012a)

$$\frac{P_{\text{mol}}}{k} = n T_{\text{eff}}. \quad (18)$$

The  $P_{\text{mol}}/k$  is derived to be  $7.3 \times 10^5 \text{ cm}^{-3} \text{ K}$  with  $n = 4.5 \times 10^3 \text{ cm}^{-3}$  and  $T_{\text{eff}} = 83 \text{ K}$ , which are obtained from the  $\text{C}^{18}\text{O}$  2–1 emission. The pressure of Sh2-152 is two orders of magnitude larger than the internal pressure of G108–S. It suggests that G108–S could be compressed by Sh2-152 if the two are physically associated. More studies are needed to confirm whether the star formation in G108–S has been indeed induced by Sh2-152. In contrast, G108–N is quiescent and seems unaffected by its surrounding environment yet.

The stability of G108–N was examined by comparing its total mass and the Jeans mass; the derived total mass is greater than the Jeans mass, indicating that G108–N is gravitationally unstable. The free-fall time ( $t_{\text{ff}} = 3.4 \times 10^7 n^{-0.5}$  yr, Evans 1999) for G108–N is about 1 Myr, which is similar to the typical lifetime of low mass starless cores with the average density of  $n \sim 10^4 \text{ cm}^{-3}$ . The lifetime for massive prestellar cores is expected to be shorter than the free-fall time (André et al. 2014). Therefore, G108–N might be about to collapse. However, it is unclear whether G108–N will survive as a single massive prestellar core or be fragmented into several components as turned out in G108–S. The peak surface densities of G108–N and G108–S are similar to  $0.07 \text{ g cm}^{-2}$  as derived from the  $\text{C}^{18}\text{O}$  1–0 line. The value is much smaller than the threshold surface density ( $1 \text{ g cm}^{-2}$ , Krumholz & McKee 2008) for fragmentation in massive star formation. The estimated surface densities of IRDCs are 0.2 to  $5 \text{ g cm}^{-2}$  (Battersby et al. 2011). However, Urquhart et al. (2014) argued that adding the effect of magnetic field could reduce the threshold of surface density for fragmentation. In addition, the distribution of surface densities of massive star-forming clumps shows that clumps with the surface density lower than  $0.1 \text{ g cm}^{-2}$  can result in high mass star formation (Figure 12 of Urquhart et al. 2014). Therefore, we cannot exclude the possibility that G108–N could form a high-mass star without fragmentation.

## 6. SUMMARY

To investigate the star formation condition near active regions such as SNRs and HII regions, various molecular line observations as well as the submm dust continuum observation toward PGCC G108.84–00.81 were carried out. Our results are:

1. One filament structure presented in the integrated intensity maps of CO 1–0 and  $^{13}\text{CO}$  1–0 is largely divided into three parts: the northeast region associated with a

star, IRAS 22576+5843, the southern region directly linked to HII region, Sh2-152, and the central part defined here as G108 containing IRAS 22565+5839. The two clumps, “G108–N” and “G108–S” are found within G108.

2. In G108–S, a blue-shifted component, whose velocity is similar to that of the component associated with Sh2-152, is shown in both of the Moment 1 maps of CO 2–1 and  $^{13}\text{CO}$  2–1. The integrated intensity ratio,  $^{13}\text{CO}$  2–1/ $^{13}\text{CO}$  1–0, is also the most enhanced at the southern edge of G108–S, which is close to the HII region.

3. Dust continuum emission also shows two components corresponding to G108–N and G108–S. Highly fragmented structures in G108–S are revealed with the beam FWHM of JCMT/SCUBA-2 ( $\sim 14''$ ). Four components, G108–S1, G108–S2, G108–S3, and G108–S4, are identified in the G108–S. G108–N has no associated IR source, while there are two IR sources corresponding with the dust continuum emission peaks, G108–S1 and G108–S2. The integrated intensity peaks of CO 2–1,  $^{13}\text{CO}$  2–1 and  $\text{C}^{18}\text{O}$  2–1 are slightly off that of dust continuum.

4. The  $\text{HCO}^+$  1–0 and HCN 1–0 show similar distributions to each other and also similar to the distribution of 850  $\mu\text{m}$  continuum emission in G108–N. The emission of two lines is distributed along the NE–SW direction with a cometary structure while  $\text{HCO}^+$  4–3 is shown only in the head part. This cometary structure is also shown in the integrated intensity map of  $\text{NH}_3$  (1,1). The centroid velocities of all lines are consistent.

5. IR sources, IRS 1 and IRS 2, associated with G108–S1 and G108–S2, respectively, are YSO candidates. IRS 1 and IRS 2 are classified as Class I sources. However, outflows associated with these Class I sources were not detected with our CO observations. Higher resolutions and better sensitivities might reveal associated outflows.

6. The  $T_{\text{ex}}$  derived from CO observations of G108–N and G108–S are 13.4 and 12.5

K, respectively. Total mass of G108–N is larger than the sum of total masses of G108 S1 to S4. The total mass of G108–N is larger than the Jeans mass, suggesting that G108–N is a prestellar clump, which is gravitationally unstable and thus a potential future star formation site.

7. Two clumps have similar properties such as the gas temperature and the  $\text{H}_2$  column density. Their chemical status does not show significant difference either although G108–N is slightly less evolved than G108–S in the view of CO depletion.

8. The gravitational fragmentation and star formation in G108-S seem induced by the compression from the HII, Sh2-152; G108–S is bent toward Sh2-152 and the CO 2–1/CO 1–0 ratio is enhanced at the bent region. In contrast, G108–N does not seem affected by its environment yet.

This work was supported by the Basic Science Research Program through the National Research Foundation of Korea (NRF) (grant No.NRF-2015R1A2A2A01004769) and the Korea Astronomy and Space Science Institute under the R&D program (Project No. 2015-1-320-18) supervised by the Ministry of Science, ICT and Future Planning. Tie Liu is supported by the KASI and EACOA fellowships. The James Clerk Maxwell Telescope is operated by the East Asian Observatory on behalf of The National Astronomical Observatory of Japan, Academia Sinica Institute of Astronomy and Astrophysics, the Korea Astronomy and Space Science Institute, the National Astronomical Observatories of China and the Chinese Academy of Sciences (Grant No. XDB09000000), with additional funding support from the Science and Technology Facilities Council of the United Kingdom and participating universities in the United Kingdom and Canada. The KVN is a facility operated by the Korea Astronomy and Space Science Institute.

## REFERENCES

- André, P., Di Francesco, J., Ward-Thompson, D., et al. 2014, *Protostars and Planets VI*, 27
- Battersby, C., Bally, J., Ginsburg, A., et al. 2011, *A&A*, 535, A128
- Bourke, T. L., Crapsi, A., Myers, P. C., et al. 2005, *ApJ*, 633, L129
- Bintley, D., Holland, W. S., MacIntosh, M., J., et al. 2014, *Proc. SPIE*, 9153, 3
- Carey, S. J., Clark, F. O., Egan, M. P., et al. 1998, *ApJ*, 508, 721
- Caselli, P., Benson, P. J., Myers, P. C., & Tafalla, M. 2002, *ApJ*, 572, 238
- Chapin, E. L., Berry, D. S., Gibb, A. G., et al. 2013, *MNRAS*, 430, 2545
- Dale J. E., Ercolano B., Bonnell I. A., 2012, *MNRAS*, 427, 2852
- Dale, J. E., Haworth, T. J., Bressert, E., 2015, *MNRAS*, 450, 1199
- Di Francesco, J., André, P., & Myers, P. C. 2004, *ApJ*, 617, 425
- Dunham, M. M., Evans, N. J., II, Bourke, T. L., et al. 2006, *ApJ*, 651, 945
- Elmegreen, B. G., & Lada, C. J. 1977, *ApJ*, 214, 725
- Evans, N. J., II 1999, *ARA&A*, 37, 311
- Evans, N. J., II, Dunham, M. M., Jørgensen, J. K., et al. 2009, *ApJS*, 181, 321
- Furuya, R. S., Kitamura, Y., & Shinnaga, H. 2006, *ApJ*, 653, 1369
- Hatchell, J., Wilson, T., Drabek, E., et al. 2013, *MNRAS*, 429, L10
- Hennebelle, P., & Chabrier, G. 2008, *ApJ*, 684, 395
- Heydari-Malayeri, M., & Testor, G. 1981, *A&A*, 96, 219



- Hildebrand, R. H. 1983, QJRAS, 24, 267
- Ishihara, D., Onaka, T., Kataza, H., et al. 2010, A&A, 514, A1
- Kim, K. T., Byun, D. Y., et al. 2011, Journal of Korean Astronomical Society, 44, 81
- Koenig, X. P., & Leisawitz, D. T. 2014, ApJ, 791, 131
- Könyves, V., André, P., Men'shchikov, A., et al. 2015, A&A, 584, A91
- Krumholz, M. R., & McKee, C. F. 2008, Nature, 451, 1082
- Lada, C. J., & Lada, E. A. 2003, ARA&A, 41, 57
- Lee, J.-E., Evans, N. J., II, and Yancy, L. Shirley 2003, ApJ, 583, 789
- Liu T., Wu Y., Zhang H., Qin S.-L., 2012a, ApJ, 751, 68
- Liu, T., Wu, Y., & Zhang, H. 2012, ApJS, 202, 4
- Liu, T., Wu, Y., & Zhang, H. 2013, ApJ, 775, L2
- Liu H.-L., Wu Y., Li J., Yuan J.-H., Liu T., Dong X., 2015, ApJ, 798, 30
- Liu, H.-L., Li, J.-Z., Wu, Y., et al. 2016a, ApJ, 818, 95
- Liu, T., Zhang, Q., Kim, K.-T., et al. 2016, ApJS, 222, 7
- Morgan, L. K., Thompson, M. A., Urquhart, J. S., et al. 2004, A&A, 426, 535
- Myers, P. C., & Ladd, E. F. 1993, ApJ, 413, L47
- Ossenkopf, V., & Henning, T. 1994, A&A, 291, 943
- Pillai, T., Wyrowski, F., Carey, S. J., et al. 2006, A&A, 450, 569
- Planck Collaboration, Ade, P. A. R., Aghanim, N., et al. 2011, A&A, 536, A23

- Planck Collaboration, Ade, P. A. R., Aghanim, N., et al. 2015, arXiv:1502.01599
- Ramírez Alegría, S., Herrero, A., Marín-Franch, A., et al. 2011, A&A, 535, A8
- Schnee, S., Caselli, P., Goodman, A., et al. 2007, ApJ, 671, 1839
- Seta, M., Hasegawa, T., Dame, T. M., et al. 1998, ApJ, 505, 286
- Simon, R., Rathborne, J. M., Shah, R. Y., et al. 2006, ApJ, 653, 1325
- Su, Y., Fang, M., Yang, J., et al. 2014, ApJ, 788, 122
- Tafalla, M., Myers, P. C., Caselli, P., et al. 2002, ApJ, 569, 815
- Tatematsu, K., Fukui, Y., Nakano, M., et al. 1987, A&A, 184, 279
- Tatematsu, K., Fukui, Y., Iwata, T., et al. 1990, ApJ, 351, 157
- Tatematsu, K., Liu, T., Ohashi, S., et al. 2017, ApJS, 228, 12
- Thompson, M. A., Urquhart, J. S., Moore, T. J. T., et al. 2012, MNRAS, 421, 408
- Ungerechts, H., Umbanhowar, P., & Thaddeus, P. 2000, ApJ, 537, 221
- Urquhart, J. S., Moore, T. J. T., Csengeri, T., et al. 2014, MNRAS, 443, 1555
- van der Tak, F. F. S., Black, J. H., Schöier, F. L., et al. 2007, A&A, 468, 627
- Whitworth, A. P., Bhattal, A. S., Chapman, S. J., et al. 1994, MNRAS, 268, 291
- Wright, E. L., Eisenhardt, P. R. M., Mainzer, A. K., et al. 2010, AJ, 140, 1868
- Wu, Y., Liu, T., Meng, F., et al. 2012, ApJ, 756, 76
- Young, C. H., Jørgensen, J. K., Shirley, Y. L., et al. 2004, ApJS, 154, 396
- Yung, B. H. K., Nakashima, J. i., & Henkel, C. 2014, ApJ, 794, 81

Zhang, T., Wu, Y., Liu, T., et al. 2016, ApJS, 224, 43

Table 1. Summary of the Observations

Molecular line	$\nu$ [GHz]	Beam FWHM [arcsec]	$\eta_{mb}$ <sup>a</sup>	Telescope
HCN 1–0	88.631847	29	0.81	IRAM 30 m
		32	0.37	KVN 21 m (Yonsei)
		33	0.43	KVN 21 m (Ulsan)
		32	0.36	KVN 21 m (Tamna)
HCO <sup>+</sup> 1–0	89.188526	29	0.81	IRAM 30 m
N <sub>2</sub> H <sup>+</sup> 1–0	93.173776	20.4	0.54	NRO 45 m
CO 1–0	115.271202	60	0.67	PMO 13.7 m
<sup>13</sup> CO 1–0	110.201354	60	0.67	PMO 13.7 m
C <sup>18</sup> O 1–0	109.782176	60	0.67	PMO 13.7 m
CO 2–1	230.538000	32.5	0.76	CSO 10 m
<sup>13</sup> CO 2–1	220.398684	32.5	0.76	CSO 10 m
C <sup>18</sup> O 2–1	219.560358	32.5	0.76	CSO 10 m
NH <sub>3</sub> (1,1)	236.94495	40	0.79	Effelsberg 100 m

<sup>a</sup>The main beam efficiencies

Table 2. Infrared Fluxes of YSO Candidates from the Archive

Source	RA ( <i>h m s</i> )	Dec ( <i>° ' ''</i> )	2MASS H (mJy)	2MASS K <sub>s</sub> (mJy)	WISE 3.4 $\mu$ m (mJy)	WISE 4.6 $\mu$ m (mJy)	AKARI 9 $\mu$ m (mJy)	WISE 12 $\mu$ m (mJy)	AKARI 18 $\mu$ m (mJy)	WISE 22 $\mu$ m (mJy)
IRS 1	22:58:34.08	+58:55:51.88	...	...	14.9 (0.2)	28.5 (0.5)	118.0 (18.6)	83.9 (1.8)	320.0 (21.0)	291.0 (6.0)
IRS 2	22:58:38.56	+58:55:48.39	2.13 (0.16)	11.1 (0.5)	41.4 (0.8)	68.9 (1.3)	107 (3.0)	88.5 (1.5)	...	196 (4.0)

Table 3. Bolometric Luminosities, Bolometric Temperatures, and IR Spectral Indices of  
IRS 1 and IRS 2

Sources	$L_{\text{bol}}$ [ $L_{\odot}$ ]	$T_{\text{bol}}$ (Class) [K]	Spectral index $\alpha$ (Class)
IRS 1	27	341 (I)	0.61 (I)
IRS 2	30	614 (I)	0.48 (I)

Table 4. Derived parameters of C<sup>18</sup>O 1–0 of G108–N and G108–S from LTE analysis

ID	$T_{\text{ex}}$ (K)	peak	mean	peak	mean	a <sup>a</sup> (arcsec)	b <sup>b</sup> (arcsec)
		$N(\text{H}_2)_{\text{C}^{18}\text{O}}$ ( $\times 10^{21} \text{ cm}^{-2}$ )	$N(\text{H}_2)_{\text{C}^{18}\text{O}}$ ( $\times 10^{21} \text{ cm}^{-2}$ )	$N(\text{H}_2)_{\text{dust}}$ ( $\times 10^{21} \text{ cm}^{-2}$ )	$N(\text{H}_2)_{\text{dust}}$ ( $\times 10^{21} \text{ cm}^{-2}$ )		
G108–N	13.4	16.1	6.7	12.3	5.6	114	40
G108–S	12.5	15.3	10.0	10.4	8.4	24	16

<sup>a</sup>The size of semi-major axis

<sup>b</sup>The size of semi-minor axis

Table 5. Total Masses of 850  $\mu\text{m}$  Dust Continuum Condensations in G108

ID	Integrated Flux Density (mJy)	Mass ( $M_{\odot}$ )
G108–N	3584.0	386
G108–S1	418.2	51
G108–S2	373.3	45
G108–S3	510.1	62
G108–S4	409.5	50

Table 6. Derived Parameters of  $\text{N}_2\text{H}^+$  1–0 from Non-LTE Calculation

ID	$T_{\text{kin}}$ (K)	$N(\text{H}_2)_{\text{dust}}$ ( $\times 10^{21} \text{ cm}^{-2}$ )	$\Delta v$ ( $\text{km s}^{-1}$ )	$N(\text{N}_2\text{H}^+)$ ( $\times 10^{14} \text{ cm}^{-2}$ )	$X(\text{N}_2\text{H}^+)$ ( $\times 10^{-8}$ )
G108–N	13.4	9.9	1.72	1.2	1.2
G108–S	12.5	7.8	2.67	1.9	2.5

Table 7. Derived parameters of HCN 1–0 from non-LTE calculation

ID	$T_{\text{kin}}$ (K)	$N(\text{H}_2)_{\text{dust}}$ ( $\times 10^{21} \text{ cm}^{-2}$ )	$\Delta v$ ( $\text{km s}^{-1}$ )	$N(\text{HCN})$ ( $\times 10^{14} \text{ cm}^{-2}$ )	$X(\text{HCN})$ ( $\times 10^{-7}$ )
G108–N	13.4	7.9	3.24	7.8	3.3
G108–S	12.5	7.4	2.53	6.5	2.9



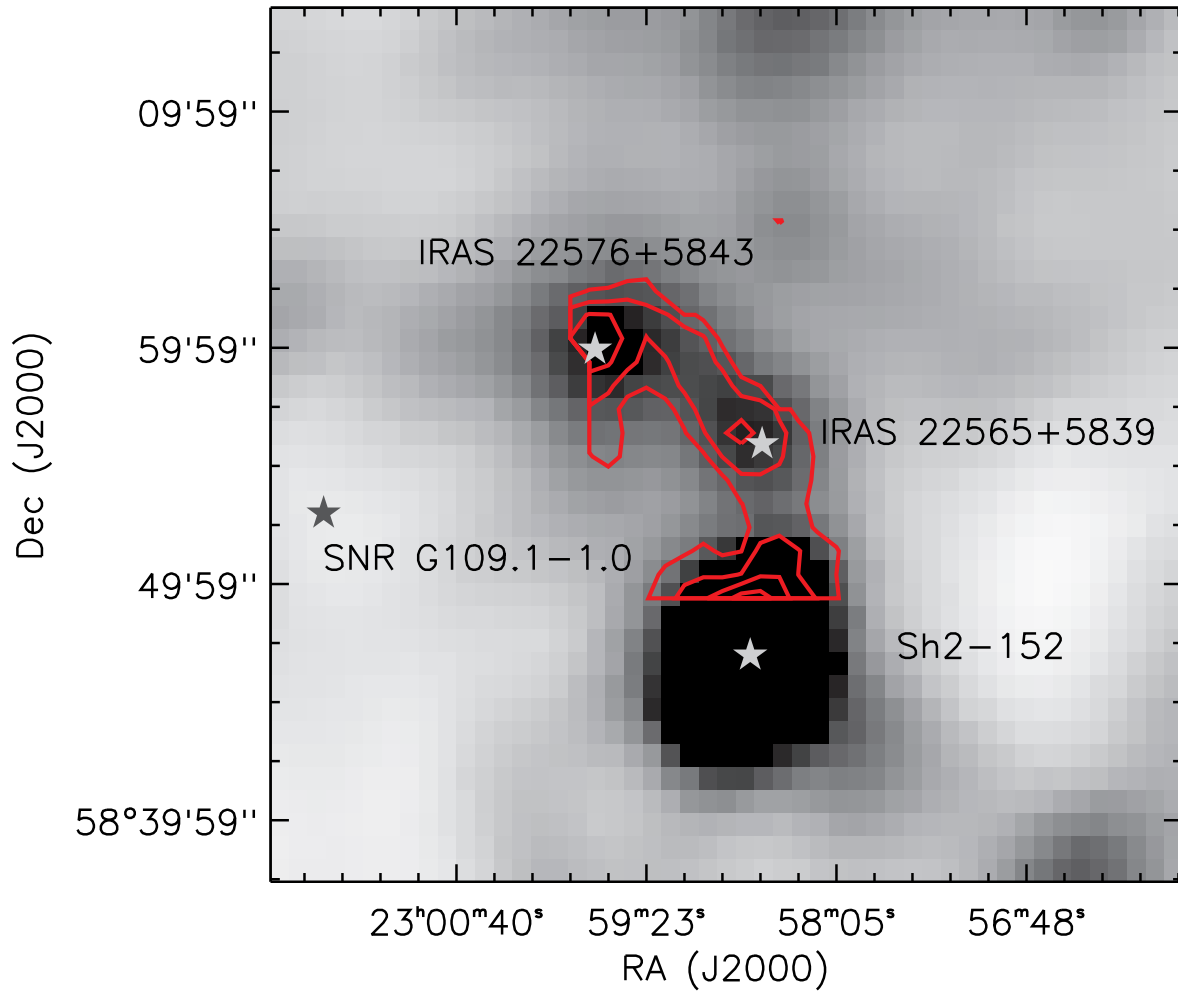


Fig. 1.— Integrated intensity maps of CO 1-0 (red contours) overlaid on *Planck* 350  $\mu\text{m}$  image (gray scale). Contour intervals are 20 % of the each peak intensity and range from 30 % to 90 %. The peak integrated intensity of CO 1-0 is  $77.5 \text{ K km s}^{-1}$ .

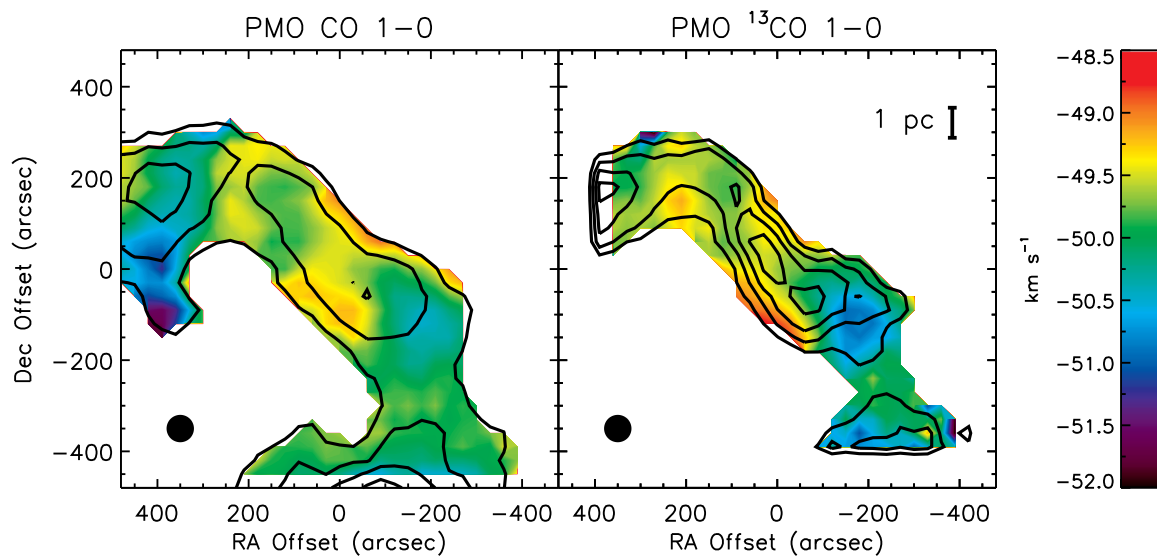


Fig. 2.— Integrated intensity maps (contours) of CO 1–0 (*left*) and  $^{13}\text{CO}$  1–0 (*right*) on top of the Moment 1 maps of CO 1–0 and  $^{13}\text{CO}$  1–0 (color scale). Contour intervals are 20 % of the each peak integrated intensity and range from 30 % to 90 %. The peak integrated intensities of CO 1–0 and  $^{13}\text{CO}$  1–0 are  $77.5$  and  $19.5 \text{ K km s}^{-1}$ , respectively. The Moment 1 maps are constructed with the data clipped using  $3\sigma$  criteria. The filled circle at the bottom-left corner of each panel denotes the respective beam FWHM of PMO 14 m.

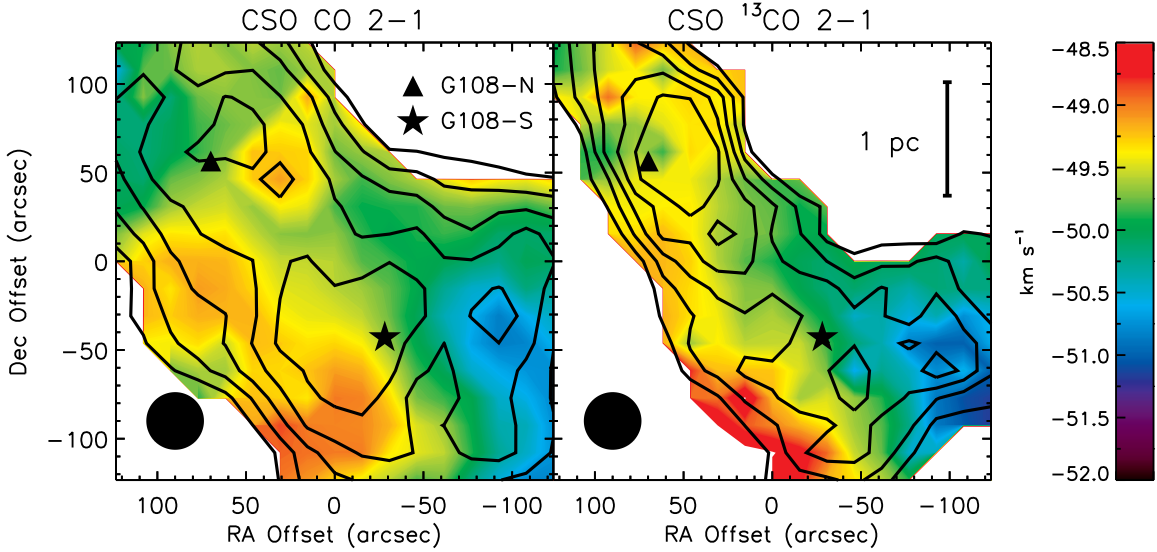


Fig. 3.— Integrated intensity maps (contours) of CO 2–1 (*left*) and  $^{13}\text{CO}$  2–1 (*right*) on top of the Moment 1 maps of CO 2–1 and  $^{13}\text{CO}$  2–1 (color scale). Contour intervals are 10 % of the each peak intensity and range from 50 % to 90 %. The peak integrated intensities of CO 2–1 and  $^{13}\text{CO}$  2–1 are 50.9 and 18.5 K km s $^{-1}$ , respectively. The Moment 1 maps are constructed with the data clipped using  $3\sigma$  criteria. The filled circle at the bottom-left corner of each panel denotes the respective beam FWHM of CSO. The positions of G108–N and G108–S are denoted by a filled triangle and star, respectively.

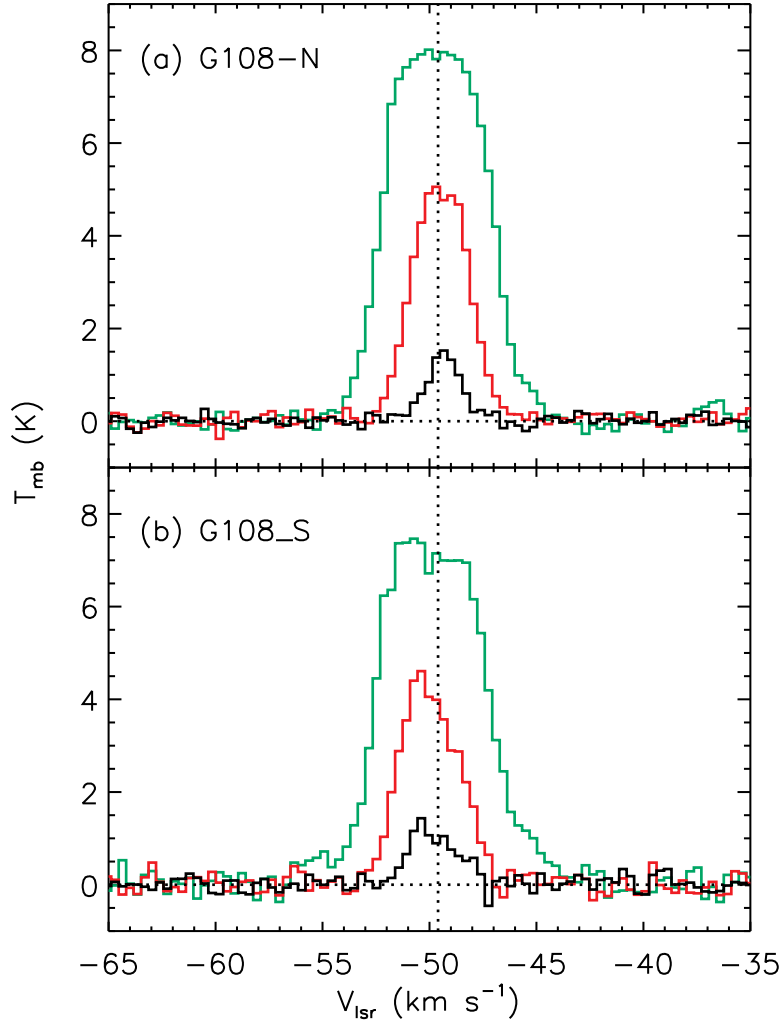


Fig. 4.— Spectra toward G108-N (*left*) and G108-S (*right*). Spectra of CO 2–1,  $^{13}\text{CO}$  2–1, and  $\text{C}^{18}\text{O}$  2–1 are presented in green, red, and black, respectively.

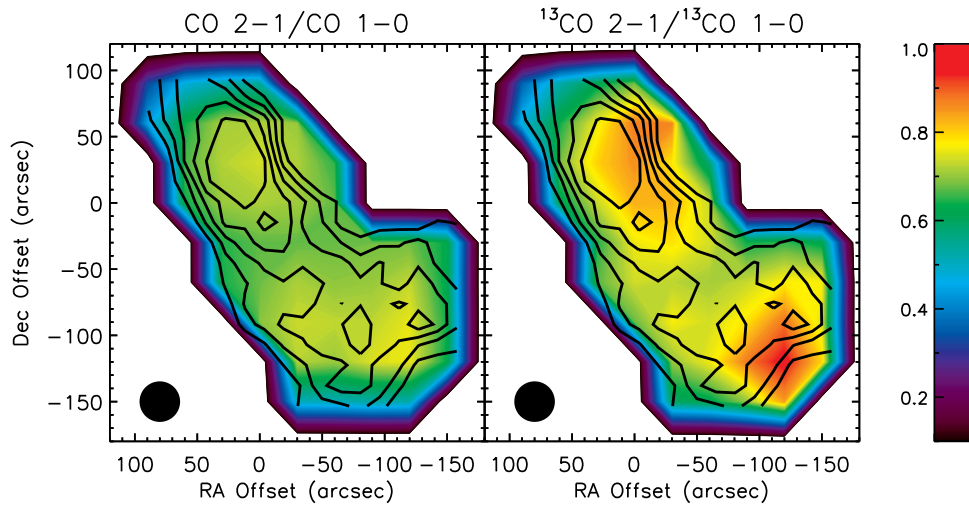


Fig. 5.— Color images show the integrated intensity ratios of CO 2–1 to CO 1–0 (*left*) and <sup>13</sup>CO 2–1 to <sup>13</sup>CO 1–0 (*right*). The black contours represent integrated intensity of <sup>13</sup>CO 2–1. The contours are the same levels as in Figure 2.

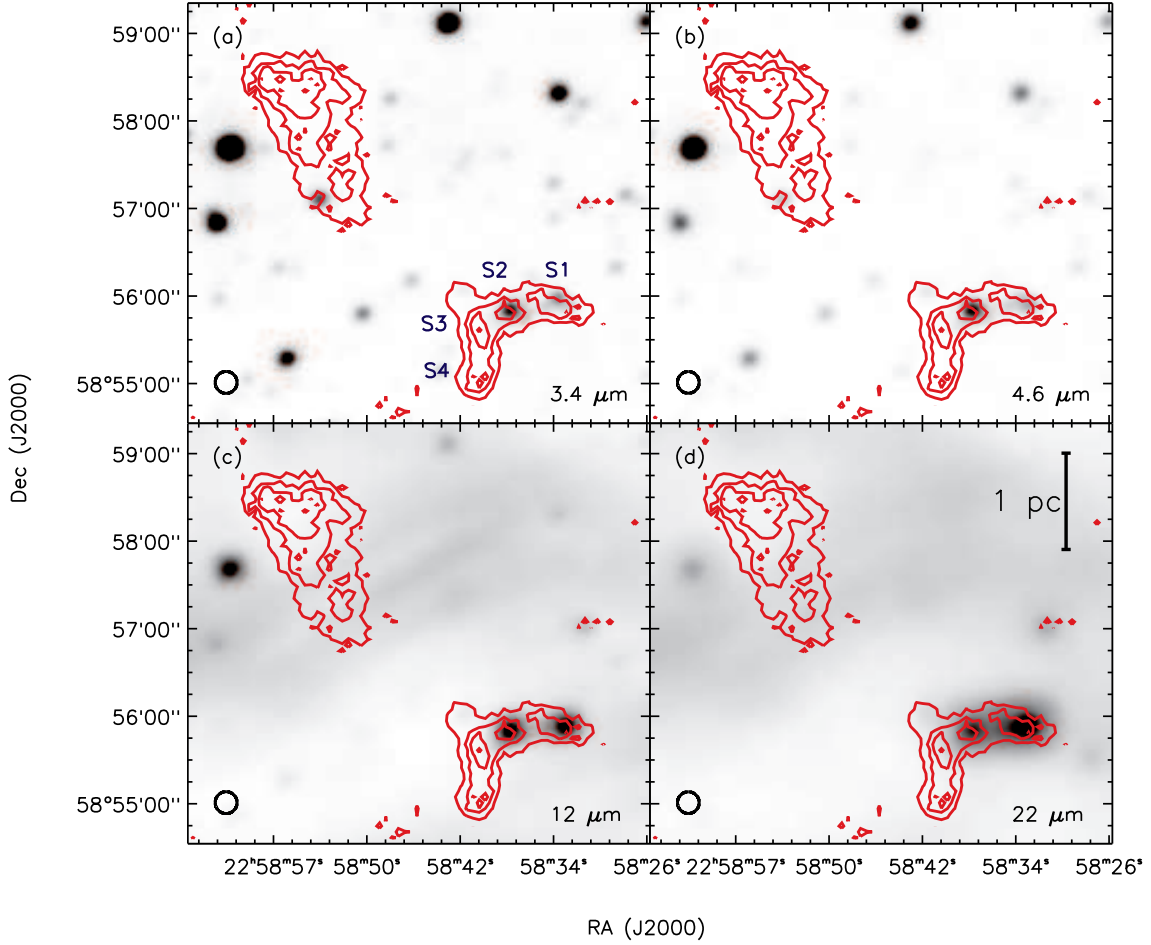


Fig. 6.— Continuum emission at  $850\ \mu\text{m}$  (red contours) overlaid on the WISE images (gray scale) at (a)  $3.4\ \mu\text{m}$ , (b)  $4.6\ \mu\text{m}$ , (c)  $12\ \mu\text{m}$ , and (d)  $22\ \mu\text{m}$ . Contour levels are 30, 50, 70, and 90 % of the peak intensity of  $232\ \text{mJy beam}^{-1}$ . The beam FWHM of JCMT/SCUBA-2 at  $850\ \mu\text{m}$  is presented with open circle.

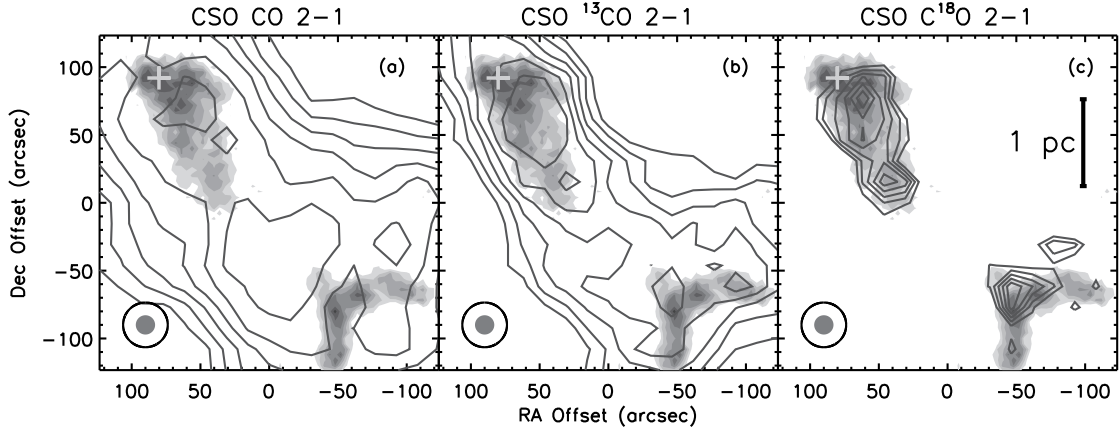


Fig. 7.— Integrated intensity maps (contours) of CO 2–1 (*left*),  $^{13}\text{CO}$  2–1 (*center*),  $\text{C}^{18}\text{O}$  2–1 (*right*) on top of the  $850\ \mu\text{m}$  dust continuum map (gray scale). Contour intervals are 10 % of the each peak intensity and range from 40 % to 90 %. The gray scale levels are 20 to 90 % of the peak intensity in step of 10 %. The peak intensities of CO 2–1,  $^{13}\text{CO}$  2–1, and  $\text{C}^{18}\text{O}$  2–1 are 50.9, 18.5, and 4.0  $\text{K km s}^{-1}$ , respectively, while the peak intensity of  $850\ \mu\text{m}$  dust continuum is  $232\ \text{mJy beam}^{-1}$ . The filled circle and the opened circle at the bottom-left corner of each panel denotes the respective beam FWHM of JCMT/SCUBA–2 and that of CSO 10 m, respectively.

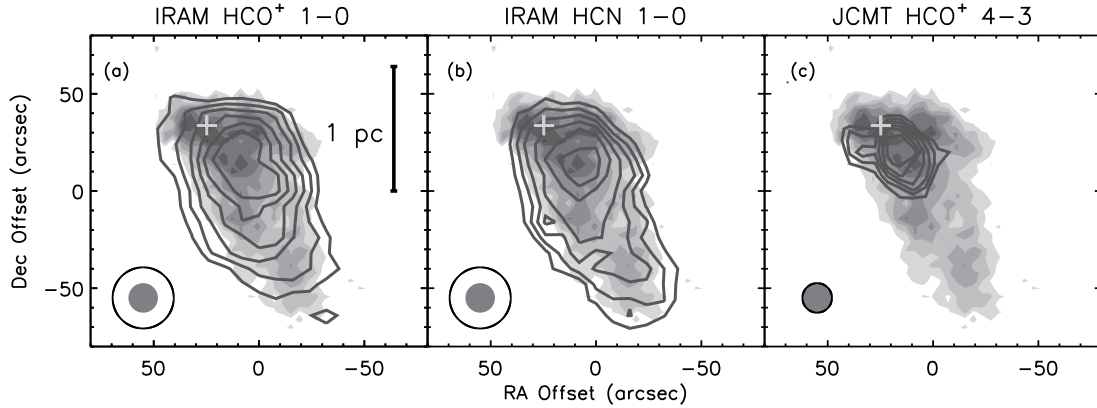


Fig. 8.— Integrated intensity maps (contours) of (a) HCO<sup>+</sup> 1–0, (b) HCN 1–0, and (c) HCO<sup>+</sup> 4–3 on top of the 850  $\mu\text{m}$  dust continuum map of G108–N (gray scale). Contour intervals are 10 % of the each peak intensity and range from 40 % to 90 %. The gray scale levels are 20 to 90 % of the peak intensity in step of 10 %. The peak intensities of HCO<sup>+</sup> 1–0, HCN 1–0, and HCO<sup>+</sup> 4–3 are 4.7, 5.6, and 0.8 K km s<sup>–1</sup>, respectively, while the peak intensity of 850  $\mu\text{m}$  dust continuum is 232 mJy beam<sup>–1</sup>. The filled circle and the opened circle at the bottom-left of each panel denotes the respective beam FWHM of JCMT/SCUBA–2 and that of IRAM 30 m, respectively.



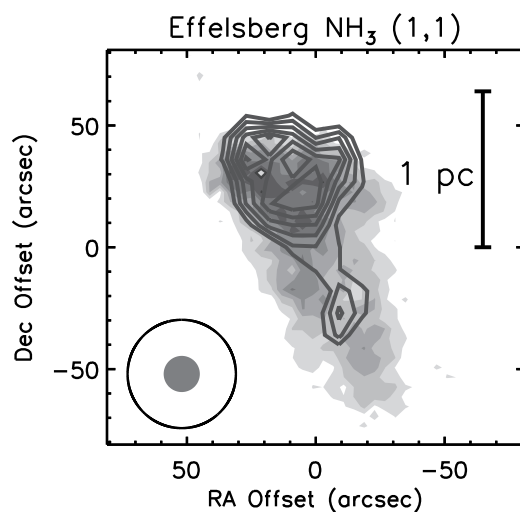


Fig. 9.— Integrated intensity map of NH<sub>3</sub> (1,1) (contours) on top of the 850 μm map of G108–N (gray scale). Contour intervals are 10 % of the each peak intensity and range from 40 % to 90 %. The gray scale levels are 20 to 90 % of the peak intensity in step of 10 %. The peak integrated intensity of NH<sub>3</sub> (1,1) is 0.54 K km s<sup>-1</sup>, respectively, while the peak intensity of 850 μm dust continuum is 232 mJy beam<sup>-1</sup>. The filled circle and the opened circle at the bottom-left of each panel denotes the respective beam FWHM of JCMT/SCUBA-2 and that of Effelsberg 100 m, respectively.

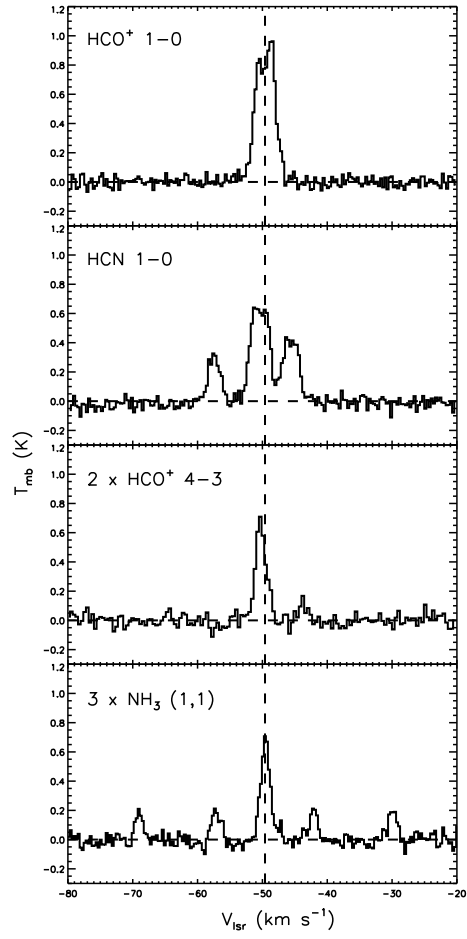


Fig. 10.— Spectra of  $\text{HCO}^+ 1-0$ ,  $\text{HCN } 1-0$ ,  $\text{HCO}^+ 4-3$ , and  $\text{NH}_3 (1,1)$  toward G108-N.

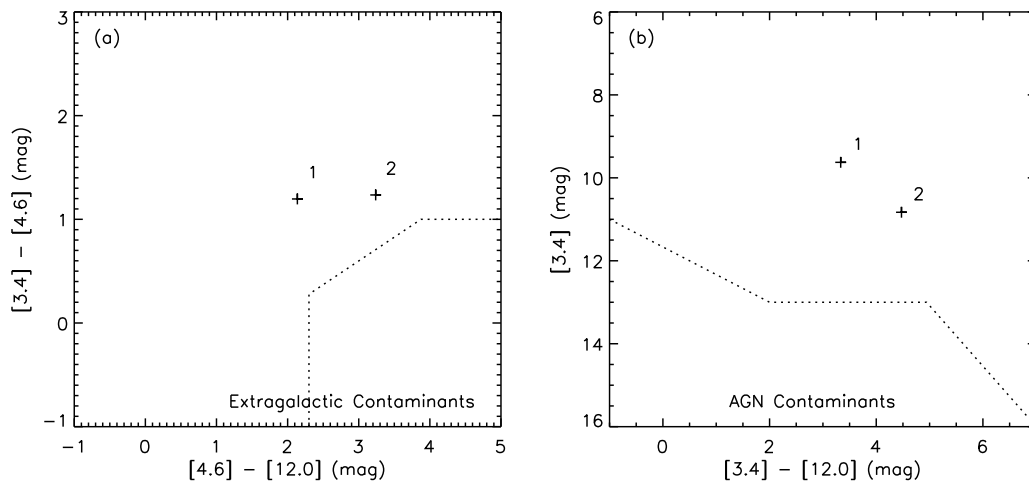


Fig. 11.— (a)  $[3.4] - [4.6]$  versus  $[4.6] - [12.0]$  color-color diagram for IRS 1 and IRS 2. The dashed lines describe the approximate criteria as likely star-forming galaxies (Koenig & Leisawitz 2014). (b)  $[3.4]$  versus  $[3.4] - [12.0]$  color-magnitude diagram for IRS 1 and IRS 2. The dashed lines indicates the region marked the approximate criteria as candidate AGNs (Koenig & Leisawitz 2014). Source numbers are labeled.

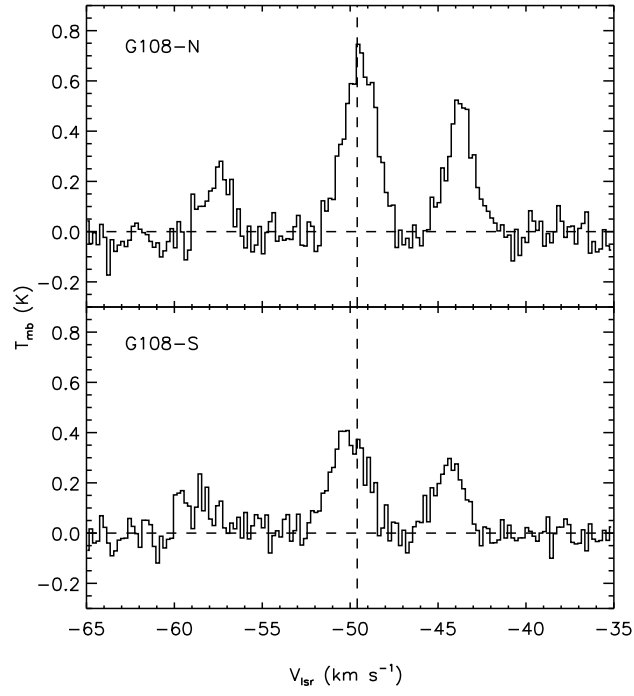


Fig. 12.— The spectra of  $\text{N}_2\text{H}^+$  1-0 toward G108-N (*upper*) and G108-S (*lower*).

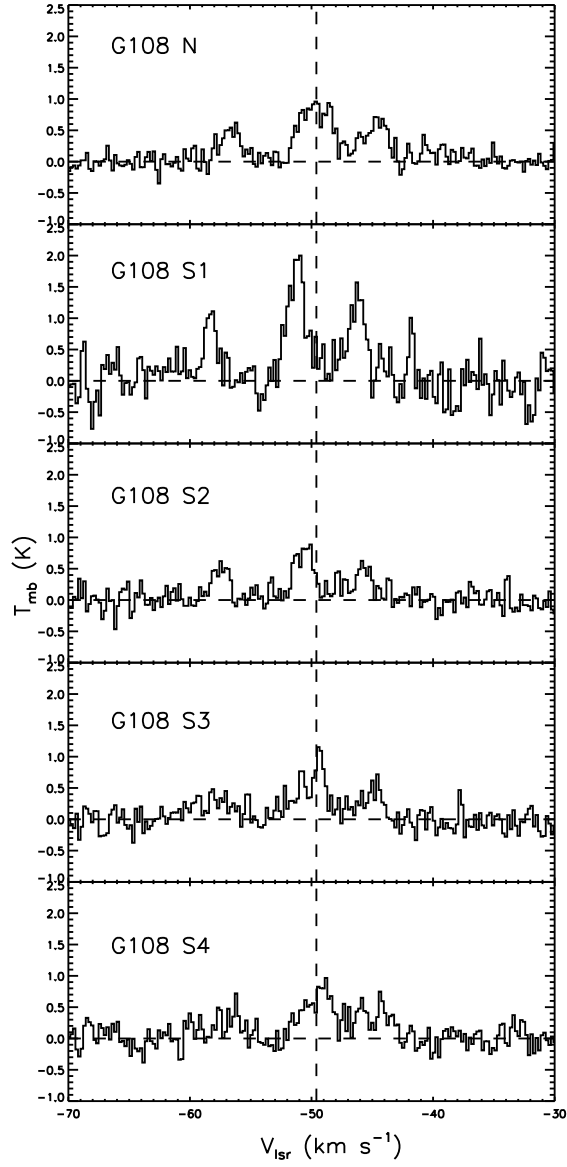


Fig. 13.— Spectra of HCN 1–0 toward G108–N, G108–S1, G108–S2, G108–S3, and G108–S4 (top to bottom).

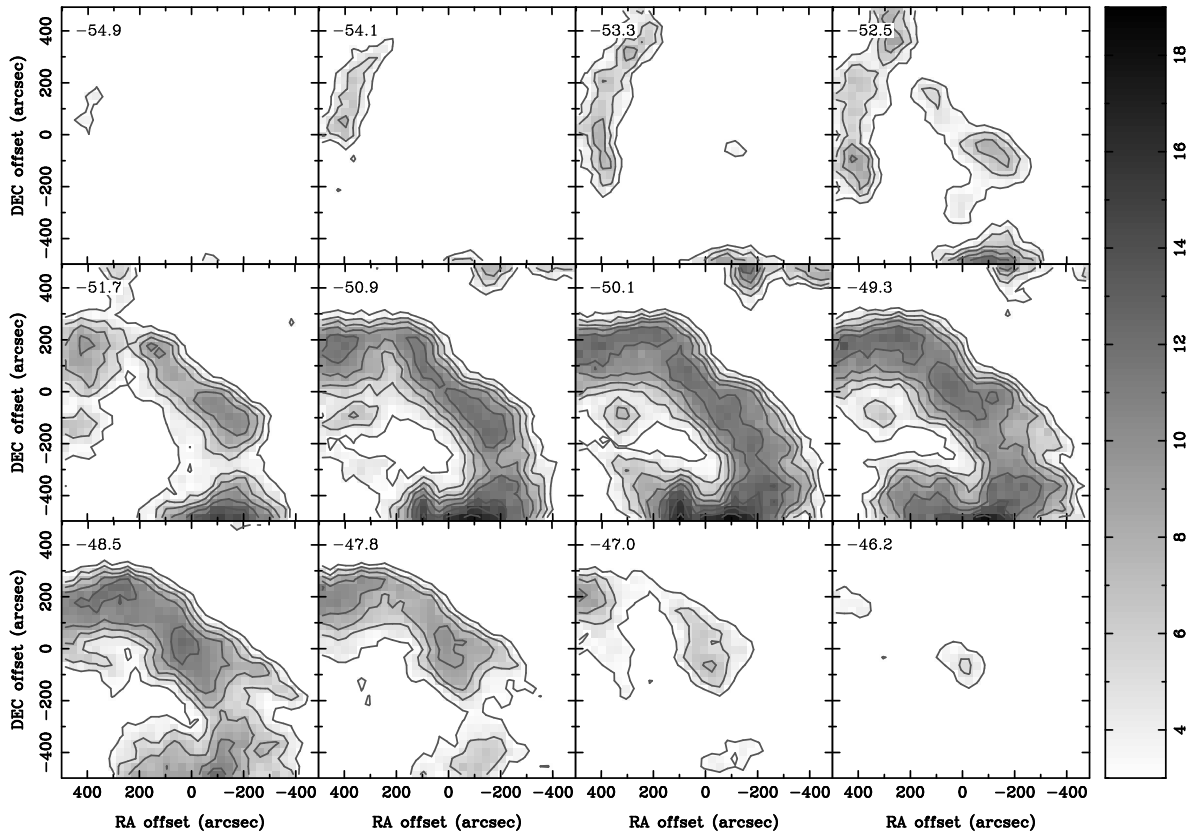


Fig. 14.— Channel maps of CO 1–0 observed with PMO. Respective velocities are indicated in the upper left of each panel in  $\text{km s}^{-1}$ . The contours are from 3 to 19 in steps of 2  $\text{K km s}^{-1}$ . The gray scale levels are from 3 to 19 in  $\text{K km s}^{-1}$ .